Nanoscale

PAPER

View Article Online
View Journal | View Issue

Cite this: *Nanoscale*, 2026, **18**, 8127

In situ X-ray imaging of segregation and mixing in PtPd core–shell nanoparticles under methane oxidation conditions

Lydia J. Bachmann, [a,b] Jagrati Dwivedi, [a] Dmitry Lapkin, †[c] Bihan Wang,[c] Jan-Christian Schober, [a,b] Gerard N. Hinsley, [c] Sarah Bernart, ‡[d] Kuan Hoon Ngoi, [c] Rustam Rysov, §[c] Arti Dangwal Pandey, [a] Thomas F. Keller, [a,b] Ivan A. Vartanyants [c] and Andreas Stierle *[a,b]

The high global warming potential of methane requires the development of advanced catalysts for conversion with increased activity and a longer lifetime. Here we utilize *in situ* Bragg coherent diffraction imaging (BCDI) to follow the evolution of two PtPd model catalyst nanoparticles during methane oxidation with different initial arrangements, one core–shell and one partially alloyed nanoparticle. While heating the nanoparticles under reaction conditions we observe the mixing and segregation of Pt and Pd, indicating a partial alloying and de-alloying, and a preferred segregation of Pt towards {111} oriented surface facets with potential use as bifunctional catalyst. Our *in situ* BCDI data also indicate a complete core–shell inversion at elevated temperatures with Pd moving into the nanoparticle. This suggests that a maximum operation temperature should not be exceeded, since Pd oxide is the more active phase. In spite of such limitations, binary metal core–shell nanoparticles are promising candidates for novel catalysts, as the elemental arrangement at their surface may be better controlled – a pivotal step for improving future catalysts.

Received 17th December 2025,
Accepted 4th March 2026

DOI: 10.1039/d5nr05321h

rsc.li/nanoscale

1 Introduction

Methane is crucial for transitioning towards a more sustainable future, for example as a carrier of hydrogen. However, due to the 28 times higher global warming potential of methane as compared to CO_2,[1] the release of any methane into the atmosphere should be avoided. Control over these emissions is therefore essential. Since the combustion of methane requires temperatures as high as 1000 °C, catalysts can instead be used for its decomposition or transformation at lower temperatures, for instance, in engines. Catalysts can change the path of the chemical reaction towards milder conditions, faster turn over frequency and increased selectivity regarding specific products. To develop catalysts with a high activity and a long lifetime, it is fundamental to understand the relationship between the structure and activity in more detail.

Common catalyst nanoparticles (NPs) for methane oxidation consist of Pd, due to the highest activity for complete methane conversion of its oxide, or Pt as it is an active methane oxidation catalyst especially at lower pressures.[2–4] Combining Pd with Pt allows to build NPs which are more stable.[5–7] The surface chemical composition is crucial for the catalyst, therefore segregation and mixing processes need to be taken into account that may alter the catalyst during operation. It is known that PtPd alloy NPs preferentially form Pd oxide at the surface under oxidizing conditions.[8] This Pd oxide formation can lead to Pd segregation to the surface, resulting in a metal Pt enriched core and a Pd oxide shell.[4,9,10] Such segregation can significantly impact catalyst properties, as demonstrated by the increased methane oxidation activity associated with Pd oxide formation.[11] The amount of the migrated Pd and the formed Pd oxide depends on the Pd to Pt ratio of the initial alloy, for very high Pt concentration less Pd oxide is formed.[4,12]

Another very important influence on the segregation and mixing process is the temperature. The maximum Pd concentration at the surface of PtPd under pure O_2 is reached at

[a]*Centre for X-ray and Nano Science CXNS, Deutsches Elektronen-Synchrotron DESY, Notkestr. 85, 22607 Hamburg, Germany. E-mail: andreas.stierle@desy.de*
[b]*Department of Physics, University of Hamburg, Notkestraße 9-11 Hamburg, 22607 Hamburg, Germany*
[c]*Deutsches Elektronen-Synchrotron DESY, Notkestr. 85, 22607 Hamburg, Germany*
[d]*Institute of Catalysis Research and Technology, Karlsruhe Institute of Technology, Hermann-von-Helmholtz-Platz 1, 76344 Eggenstein-Leopoldshafen, Germany*
†Current address: Institute of Applied Physics, University of Tübingen, 72076 Tübingen, Germany.
‡Current address: Inorganic Materials and Catalysis, Eindhoven University of Technology, 5600 MB Eindhoven, Netherlands.
§Current address: European X-ray Free-Electron Laser Facility, Holzkoppel 4, 22869 Schenefeld, Germany.

about 500 °C (thermodynamic equilibrium), at higher temperatures the Pd concentration at the surface is decreasing.[12] To determine the composition inside the NPs, strain measurements can give insights, since both elements have different lattice constants with a mismatch of 0.8% at room temperature (RT).[13–16] A powerful method to investigate the strain on the nanometer scale is Bragg coherent diffraction imaging (BCDI), which enables to measure the shape and the strain inside single NPs *in situ* with a spatial resolution of about 5 nm.[17–21]

Apart from the increased stability, the combination of two materials can influence the activity. It has been shown, that core–shell systems can have different strain and electronic properties compared to pure or alloyed materials, which might boost the catalytic activity.[22–25] In the present work we compare the mixing and segregation behavior of an initial core–shell NP with an initially partially alloyed NP under methane oxidation conditions at various temperatures between RT and 680 °C. We influenced the initial state by increasing the temperature of the second sample during the overgrowth with Pd, resulting in Pd diffusion into the NP. While the initial core–shell NP showed a facet orientation dependent segregation of Pt towards the {111} oriented facets between 470 °C and 560 °C during methane oxidation, the initially partially alloyed NP did not show such segregation behavior. At the final temperature (620 °C) at which the core–shell sample was analyzed, it was observed that Pd and Pt started to mix. Heating the initially partially alloyed NP to even higher temperatures (680 °C) revealed that the Pt is segregating to the surface, leading to a Pt shell and Pd rich core. These compositional changes at the surface are expected to have a high influence on the catalytic activity of the NPs.

2 Experimental

2.1 Sample preparation

Two 0.5 wt% Nb doped single crystal strontium titanate (STO) (100) substrates were cleaned by buffered oxide etch and annealed in a tube furnace at 950 °C for 1 h in air.[26,27] Both investigated samples were prepared by electron beam lithography (EBL), similar to that described in ref. 27. Thereby, a 50 nm thick Pt film was deposited on the STO and then the whole surface was coated with a resist film of AR-N 7520 and softbaked at 85 °C for 90 s. Afterwards, the markers and nanodots with sizes between 30–200 nm were written by the electron beam in a pattern as shown in SI section S1 (both samples had slightly different patterns). Then, the resist was developed in AR 300-47 for 1 min, stopped in de-ionised water for 30 s and postbaked at 75 °C for 1 min, leading to a removal of the resist besides the desired areas, where the electron beam was applied. Next, the Pt was removed by Ar plasma etching everywhere, wherever it was not protected by the resist. The rest of the resist got removed by a solvent remover, followed by an ultrasonic bath in acetone and isopropanol for 1–2 min and at the end by O_2 plasma cleaning for 10 min at 300 W and a O_2 flow of 145 SCCM.

The treatment after the EBL procedure was performed at the DESY NanoLab.[28] Sample-150 was annealed in air at 950 °C for 2 h. Then Sample-150 was brought into UHV and annealed for 1 h at 410 °C, cleaned in 1×10^{-6} mbar O_2 for 30 min at 410 °C, annealed again for 30 min at 410 °C and finally overgrown with Pd at 150 °C for 13 min. This procedure resulted in a nominal Pd thickness around (1.7 ± 0.7) nm as the calculations in SI section S2 show and a diffusion length of around 1.5×10^{-12} nm shown in SI section S3. Sample-670 on the other hand, was annealed in UHV by very slowly ramping to 1100 °C and keeping it at this temperature for 15 min. The sample was taken out of UHV conditions, to test the quality of such EBL samples for BCDI experiments at beamline P10 under N_2 flow at RT. Afterwards, Sample-670 was annealed in UHV for 90 min at 670 °C and then overgrown with Pd at 670 °C for 1 h. This sample has a higher nominal thickness of (4.9 ± 0.2) nm and a much larger nominal diffusion length of around 0.4 nm as it is a function of the temperature and time, as described in SI sections S2 and S3.

2.2 *Ex situ* characterization techniques

The samples were investigated by high-resolution field-emission Scanning Electron Microscope (SEM) to pre-select NPs and to characterize their diameter. Different imaging modes were used, including a through-the-lens detector with backscattered electrons of 5 kV for (Fig. 1e) and an Everhart–Thornley detector for the secondary electron mode with 5 kV for (Fig. 1a and b). To characterize the sample heights, Atomic Force Microscopy (AFM) in tapping mode was used. The measurements were performed in air, with an oxide-sharpened silicon nitride cantilever. Different resolutions and scanning rates were used, 256 × 256 px with 1 Hz on Sample-150 and 1024 × 1024 px with 0.5 Hz on Sample-670. A plane fit algorithm was used to correct for any possible macroscopic sample tilt.

2.3 Bragg coherent diffraction imaging

The *in situ* BCDI experiment was performed at the coherence applications beamline P10 of PETRA III synchrotron with a photon beam energy of 13.09 keV, using CRLs to get a coherent illumination of 0.8 × 1.2 μm^2 ($v \times h$). An EIGER X 4M detector with a pixel size of 75 × 75 μm^2 was mounted on the arm of a six circle diffractometer.[29] The sample-detector distance was measured to be 1833 mm, enabling the required diffraction peak resolution. To find the Pt markers and consequently the pre-selected NPs, the sample was mapped on the Pt(111) Bragg peak. The Bragg angle of Pt(111) at this energy is 12.1°, resulting in an illumination footprint of around 3.8 μm. Each dataset contains a scan with an angular range of ±0.4° to ±0.6° with a step-size of 0.01°, an exposure time of 10 s per step and a realignment at every fifth step.

To retrieve the crystalline real space shape from each dataset, the collected images were stacked and cut to individual region of interests, centered around the (111) Bragg peak as displayed in SI section S6. Then, an iterative phase retrieval algorithm was applied *via* the software PHASOR.[30] Thereby, different algorithm sequences were used. On Sample-670 either four cycles of 300 iterations difference map (DM) fol-

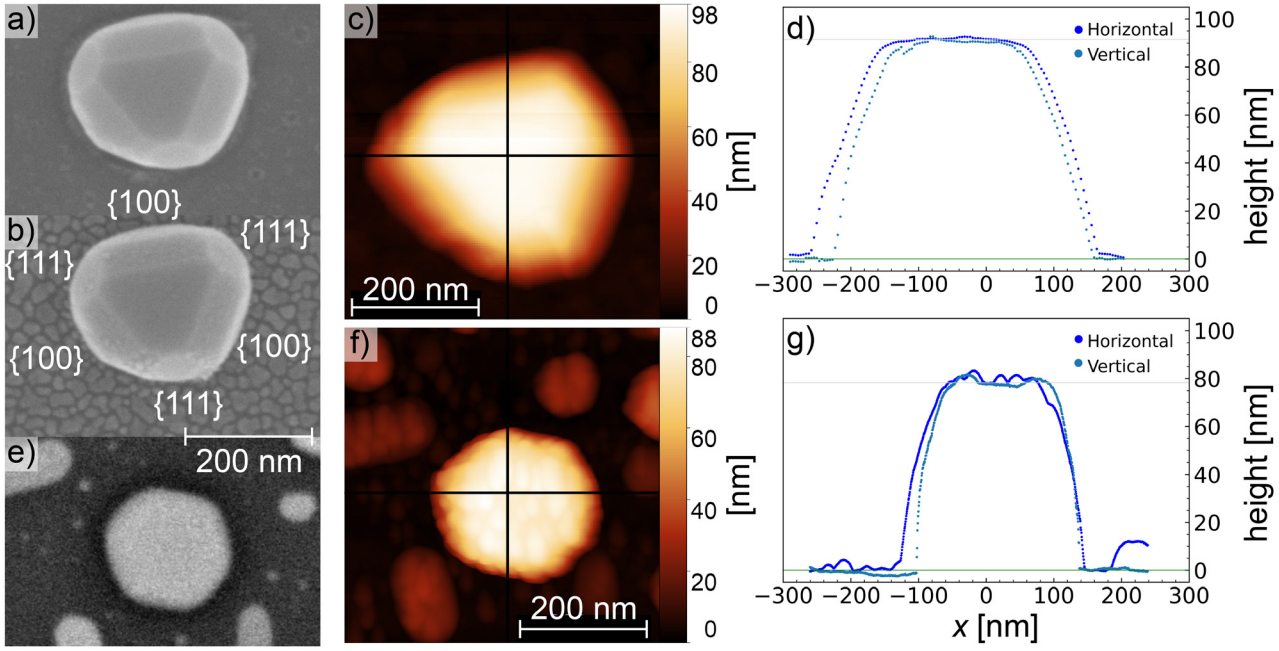

Fig. 1 Initial architecture of the investigated NPs (a–d) Sample-150: (a) SEM image before and (b) after overgrowth with Pd at 150 °C. (c) AFM image after the overgrowth and (d) AFM height profile obtained from (c) used to determine the NP height of (91 ± 1) nm. (e–g) Sample-670: (e) SEM image after Pd overgrowth at 670 °C. (f) AFM image after the overgrowth and (g) height profile obtained from AFM image in (f), the determined height is (78 ± 1) nm.

lowed by 300 iterations error reduction (ER) or three cycles of 300 iterations hybrid input–output (HIO) followed by 300 iterations ER or three cycles of 300 iterations DM followed by 300 iterations ER were used, all with a shrink-wrap threshold of 0.2. For Sample-150 the reconstruction was more difficult, since the high strain of the core–shell structure made it more challenging for the algorithm to converge, so additionally to the same sequences as on Sample-670 also the shrink-wrap threshold was adapted between 0.07 and 0.2 for each dataset. The sequences for each dataset are listed in SI section S6. Afterwards, the results of the phase retrieval algorithm were transformed into laboratory coordinates and the ten best reconstructions were selected and averaged. The voxel size in each reconstruction for Sample-670 is approximately $5 \times 5 \times 5$ nm^3, while for Sample-150 it is approximately $7 \times 3 \times 3$ nm^3. Due to the different ROI and angular ranges, the voxel size in each dataset differs slightly. The final values are listed in SI section S6.

The strain ε_{zz} is defined along the (111) direction, so the scattering vector $\boldsymbol{g}$ is parallel to the z-axis. With $\varepsilon_{zz}(r) = \partial u_z(r)/\partial z$ the strain can be calculated from the displacement field $u(r)$. This displacement field is connected to the reconstructed phase of the real space object by $\Phi(r) = -u(r)\cdot\boldsymbol{g}$, so it follows $u(r) = -\Phi(r)/|\boldsymbol{g}| = -\Phi(r)/(2\pi/d_{hkl}) = -d_{hkl}\Phi(r)/(2\pi)$ with the distance d_{hkl} between the lattice planes in (hkl) direction. So for the 111 Bragg peak $d_{hkl} = a_{\mathrm{NP}}/\sqrt{3}$ with a_{NP}, determined from the Bragg peak position as described in SI section S7. A discussion of the strain error can be found in SI section S12.

For comparability the limits of the color scales in this manuscript were set to ±0.334% for all images displaying the strain. This limit was chosen by taking the average strain of a dataset with high strain values (dataset 22 on Sample-670) and adding the standard deviation to it.

2.4 *In situ* set-up

A custom made gas dosing system was used to provide the gases and temperatures for the *in situ* experiment.[16,31] This system includes a flow reactor with Be dome which is equipped with water cooling to reduce thermal expansion during the controlled sample heating. The sample was heated to temperatures between RT and 810 °C, using the temperature calibration shown in SI section S14. The gas flow was controlled by calibrated massflow controllers, one for each gas.

Throughout the experiment a total pressure of 0.1 bar with a total flow of around 50 mL min^{-1} was applied. Three different gas mixtures were flown to the reactor: either 50 mL min^{-1} Ar (hereafter referred to 'Ar atmosphere') or 48 mL min^{-1} Ar + 2 mL min^{-1} H_2 ('H_2 treatment') or 28.5 mL min^{-1} Ar + 2.6 mL min^{-1} CH_4 + 20 mL min^{-1} O_2 ('methane oxidation conditions'). Detailed gas and temperature conditions can be found in SI section S9 for both samples.

3 Results

3.1 State of as prepared NPs

Both investigated samples were prepared by EBL, as described in the Experimental section, producing isolated Pt NPs arranged in a regular array on the single crystal STO (100)

support. Pt fiducial markers, shown in SI section S1, facilitated locating the same NPs during pre- and postprocessing, as well as during the *in situ* experiment. The samples were then overgrown with Pd, Sample-150 at 150 °C and Sample-670 at 670 °C. The different overgrowth temperatures, times and deposition rates resulted in different nominal Pd thicknesses, (1.7 ± 0.7) nm for Sample-150 and (4.9 ± 0.2) nm for Sample-670 (see SI section S2). Correspondingly, the nominal diffusion lengths were 1.5×10^{-12} nm and 0.4 nm, respectively (see SI section S3, neglecting surface induced segregation effects). Since the diffusion length on Sample-150 is close to zero, we expected a Pd layer on the Pt NP, while the diffusion length on Sample-670 is sufficient to allow some Pd diffusion into the Pt NP, forming a partially alloyed NP. On both samples, a well shaped NP was selected for comprehensive *ex situ* and *in situ* investigations. The results from the pre-characterization of the NP on both samples are displayed in Fig. 1.

Comparing the SEM images on Sample-150 before and after the Pd overgrowth (Fig. 1a and b), reveals small Pd NPs on the substrate and the Pt NP side facets. In contrast, an SEM image of Sample-670 after Pd overgrowth (Fig. 1e) does not show similar Pd NPs on the substrate or the Pt NP, indicating that the higher overgrowth temperature either produced a smooth Pd film or caused Pd diffusion into Pt. Furthermore, the {100} facets on Sample-150 are larger than the {111} facets resulting in a more triangular shape, while Sample-670 has a more hexagonal shape and the facet orientation is not identifiable in the SEM image. Regarding particle dimensions, Sample-150 has a diameter of 275–283 nm and is therefore around 100 nm larger than Sample-670 with a diameter of 179–195 nm. The heights of the particles were determined by AFM, shown in (Fig. 1c and 1f). The line profiles extracted from these AFM images, shown in (Fig. 1d and 1e), identify that Sample-150 has a height of (91 ± 1) nm, and is approximately only 13 nm taller than Sample-670 which has a height of (78 ± 1) nm. The measured height and diameter together with the nominal thickness of the overgrown Pd, lead to an estimated nominal volume fraction of 2 vol% Pd and 98 vol% Pt on Sample-150 assuming a complete coating and a simplified NP shape, as shown in SI section S4. Similarly, Sample-670 has an estimated nominal volume fraction of 6 vol% Pd and 94 vol% Pt.

The initial state of the NPs was also characterized by BCDI. Thereby, the intensity distribution around the 111 Bragg peak was measured by scanning the incident angle in a range of ±0.4° to ±0.6°, as explained in the Experimental section. The height of the crystalline part of the NPs can be calculated from the fringes of this intensity distribution as discussed in SI section S5, resulting in heights of (97 ± 7) nm for Sample-150 and (77 ± 3) nm for Sample-670. These are in good agreement with the heights measured by AFM. Applying phase retrieval algorithms to the measured intensity distributions allows to reconstruct the shape and strain of the crystalline part of the NPs, as described in the Experimental section. The reconstructed shapes of both initial NPs are shown in (Fig. 2a and 3a), for Sample-150 and Sample-670, respectively, which agrees well with the shapes measured by SEM and AFM. A list with the specific applied algorithms for each dataset can be found in SI section S6.

The initial strain distribution at RT and under Ar atmosphere (50 mL min^{-1}) is shown in Fig. 2 for Sample-150. The strain was calculated as described in the Experimental section with the lattice constant a_{NP} = (3.920 ± 0.001) Å calculated from the observed Bragg peak position. The most distinctive feature is the high tensile strain (positive sign) inside the NP and the compressive strain (negative sign) towards the surface. This is clearly visible by the two peaks in the histogram (Fig. 2f) of the strain values of the cut shown in (Fig. 2e), which can be fitted by two Gaussian functions as described in SI section S8. Such bimodal strain distributions can be observed when investigating core–shell materials.[13–15] In this case, we associate compressive strain in Pd rich and tensile strain in Pt rich regions, because a_{Pd} = 3.890 Å < a_{NP} < a_{Pt} = 3.923 Å. We calculate the strain from the lattice constant a_{Pt} of Pt relative to the lattice constant a_{NP} from the measured Bragg peak position, using the strain definition shown in SI section S7. For the initial state, this results in a tensile strain of (0.08 ± 0.02)%. This is the same order as the mean of (0.165 ± 0.006)% fitted in the histogram which indicates that the areas with tensile strain are regions of pure Pt. For a region with 100% Pd, the compositional strain would be (−0.77 ± 0.02)% compared to a_{NP}. This strain value is significantly lower than the mean of (−0.032 ± 0.009)% fitted for the second peak in the strain histogram and even lower than the minimum strain value of around −0.25%. This discrepancy is related to the difference between the observed thickness of the compressive strain ring of (27 ± 9) nm, and the much smaller nominal thickness of the evaporated Pd of (1.7 ± 0.7) nm. Both is an indication that the observed ring of compressive strain is not only compositional strain from the Pd shell, but primarily mechanical strain in the Pt whose lattice is adapting to the Pd shell. Similar lattice changes of the core material to the shell material has been shown in previous studies.[15,32,33] This effect of the overgrown shell material on the core lattice depends on several parameters. First, the lattice mismatch between both metal materials cannot be larger than 5%. Otherwise, epitaxic growth of the shell material on the core can be excluded.[32] The lattice mismatch between Pt and Pd of 0.8% is much smaller than this limit. Second, the shell material should be able to grow epitaxially on the core material if the temperatures during and after the overgrowth are low enough to suppress any inter-diffusion. For Sample-150 the overgrowth temperature was 150 °C, which does not imply any diffusion. Third, the thickness of the overgrown layer must be below a critical thickness, otherwise the shell lattice will incorporate dislocations rather than expanding or compressing the core lattice. The critical thickness h_c for coherent growth of Pd on Pt is calculated to be around 56 nm at RT as described in SI section S13. The nominal thickness of Pd on Sample-150 is (1.7 ± 0.7) nm, far below this critical thickness. Simulations of Pd on Au have shown that, if all three conditions are fulfilled, an evaporated layer of 4 nm Pd can have an influence on the

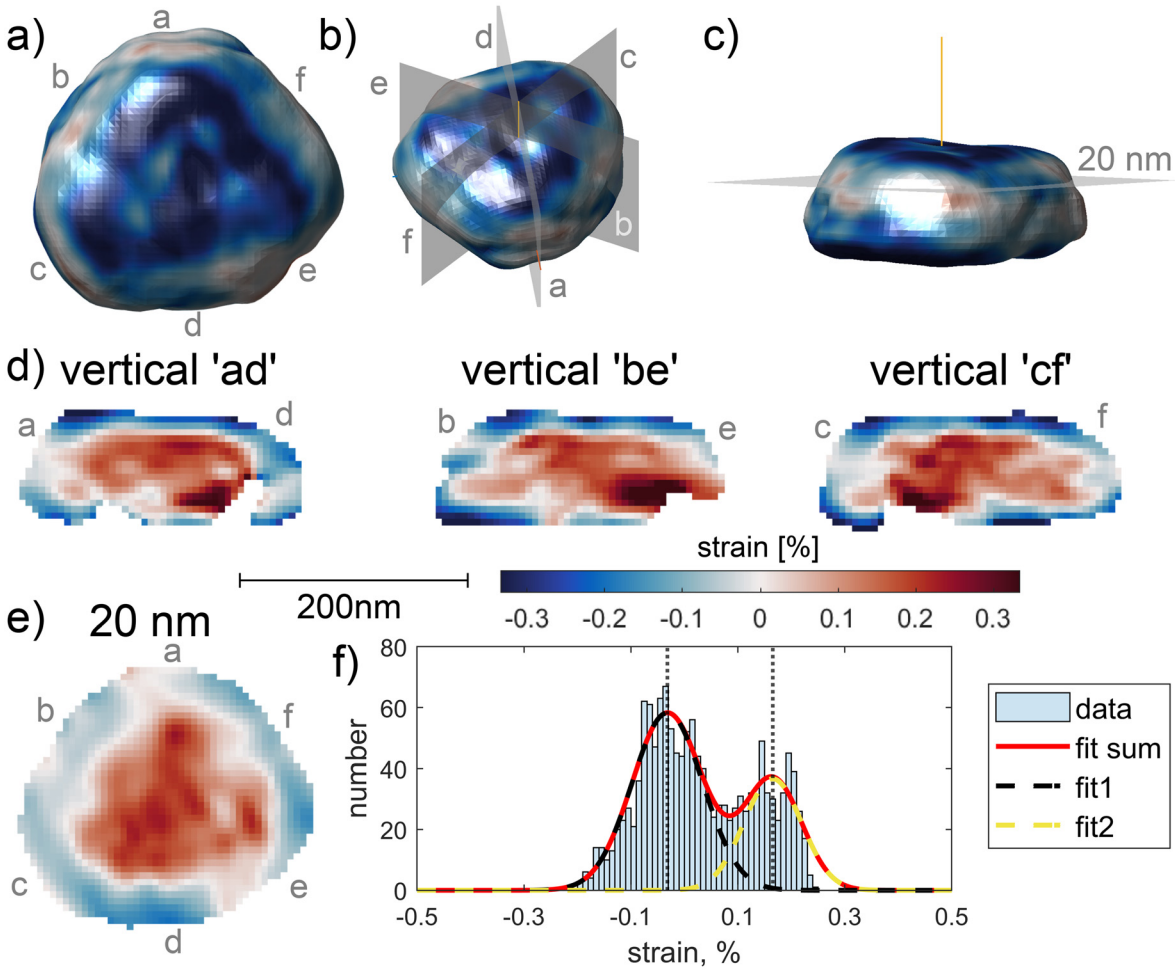

Fig. 2 Initial strain and shape of Sample-150 (a) Top view of the reconstructed strain, (b) inclined view with the planes of the cuts displayed in (d) and (c) side view with a plane indicating the cut displayed in (e). (d) Vertical cuts to the substrate and perpendicular to the facets as shown in (b). (e) A horizontal cut to the substrate, 20 nm above the center of mass of the reconstruction, as shown in (c). (f) Histogram of the strain values from the cut shown in (e), fitted by two Gaussians. The dotted vertical lines indicate the fitted peak positions of (−0.032 ± 0.009)% and (0.165 ± 0.006)%. For all images, an isosurface value of 0.2 was used. The displayed dataset was measured at RT and under Ar atmosphere. The gaps in the reconstructed shape do not result from real gaps in the NP, but rather from failure in the reconstruction at those points. The letters a-f used to label the facets are consistent across all images.

lattice constant of an Au core up to 20 nm inside the NP, which agrees well with our observation.[32]

The initial strain distribution of Sample-670 is shown in Fig. 3 and the strain was calculated with the lattice constant a_{NP} = (3.920 ± 0.001) Å from the observed Bragg peak position, which is identical to the lattice constant of the initial state of Sample-150. In comparison to Sample-150 the strain in Sample-670 is more mixed, with positive and negative strain values in the center and near the surface. The origin of this non core–shell structure in Sample-670 lies in the higher overgrowth temperature, which resulted in Pd diffusion into the Pt NP. Although the calculated diffusion length on Sample-670 is still smaller than the nominal Pd thickness of (4.9 ± 0.2) nm, it was sufficient to reduce the strain induced by the overgrown Pd. Simultaneously, also Pt surface segregation can occur.[34]

3.2 *In situ* structural changes during methane oxidation

During the *in situ* experiment, both samples were exposed to three different gas conditions: Ar atmosphere, H_2 treatment and methane oxidation condition, as defined in the Experimental section. Under these gas conditions, temperatures ranging from RT to 680 °C were applied. Detailed condition sequence with time and acquired BCDI datasets for both samples can be found in SI section S9.

Fig. 4 displays the reconstructed shape of a selection of datasets on Sample-150, showing some changes throughout the *in situ* experiment. Foremost, when comparing (Fig. 4a) to (Fig. 2), the strain at the top facet has an opposite strain. This change of sign appears after elevating the temperature to 470 °C and exposing the sample to methane oxidation condition for the first time. It was not possible to measure under

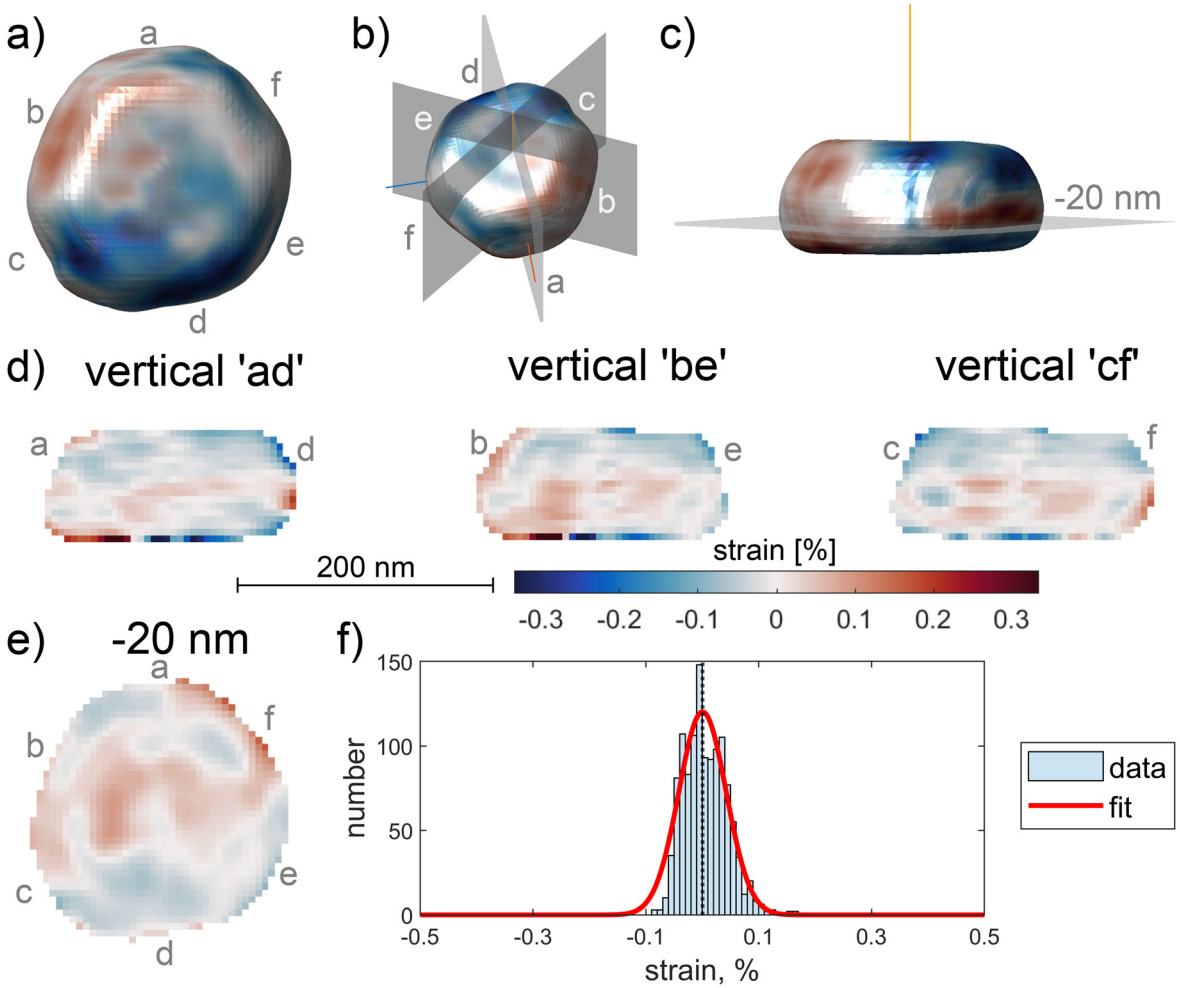

Fig. 3 Initial strain and shape of Sample-670. (a) Top view of the reconstructed strain, (b) inclined view with the planes of the cuts displayed in (d) and (c) side view with a plane indicating the cut displayed in (e). (d) Vertical cuts to the substrate and perpendicular to the facets as shown in (b). (e) A horizontal cut to the substrate, −20 nm relative to the center of mass of the reconstruction, as shown in (c). (f) Histogram of the strain values from the cut shown in (e), fitted by one Gaussian. The dotted vertical line indicates the fitted peak position of (0.000 ± 0.004)%. For all images, an isosurface value of 0.2 was used. The displayed dataset was measured at RT and under Ar atmosphere. The letters a-f used to label the facets are consistent across all images.

this condition due to experimental issues, instead the dataset displayed in (Fig. 4a) was measured at RT and under Ar atmosphere after this first exposure. The tensile strain at the top facet indicates Pt segregation through the Pd shell to the surface of the top facet. A H_2 treatment at 320 °C was leading to Pt segregation towards other facets as (Fig. 4b) shows. This is in line with previous findings, showing that H_2 treatment at elevated temperatures promotes the movement of Pt atoms to the surface in PtPd NPs.[34] As the black arrows in (Fig. 4b) indicate, the Pt only segregated to the {111} facets. Similar facet orientation dependent segregation behavior towards {111} oriented facets was observed for a PtRh NP under CO conditions.[16] In our case, Pt stayed at the {111} facets, after switching back to methane oxidation conditions and ramping the temperature to 520 °C. Only after increasing the temperature further to 560 °C, Pt disappeared from the surfaces, as (Fig. 4c) shows. This could be related to preferred Pd segregation and surface oxide formation at this condition.[12] The strain inside the NP stays the same, unaffected by the Pt segregation to the {111} facets and back, as the horizontal (−20 nm) and the vertical ('cf') cuts in Fig. 4 show.

When increasing the temperature further to 620 °C, the strain at the surface and inside the NP decreases, as seen in the vertical and horizontal cuts in (Fig. 4d). This decrease of the strain could be the first step towards the disappearance of the core–shell structure, as the ring structure in the horizontal cut nearly vanished. The fits of the histograms support this assumption, since one Gaussian in (Fig. 4f), instead of two in (Fig. 4e), is sufficient to fit the histogram and results in decreasing mean values from −(0.163 ± 0.018)% and (0.044 ± 0.005)% at 560 °C to (0.015 ± 0.006)% at 620 °C. Additionally, the minimal values in the cuts are getting higher, from −0.33% to −0.2%. Additional values and histograms are

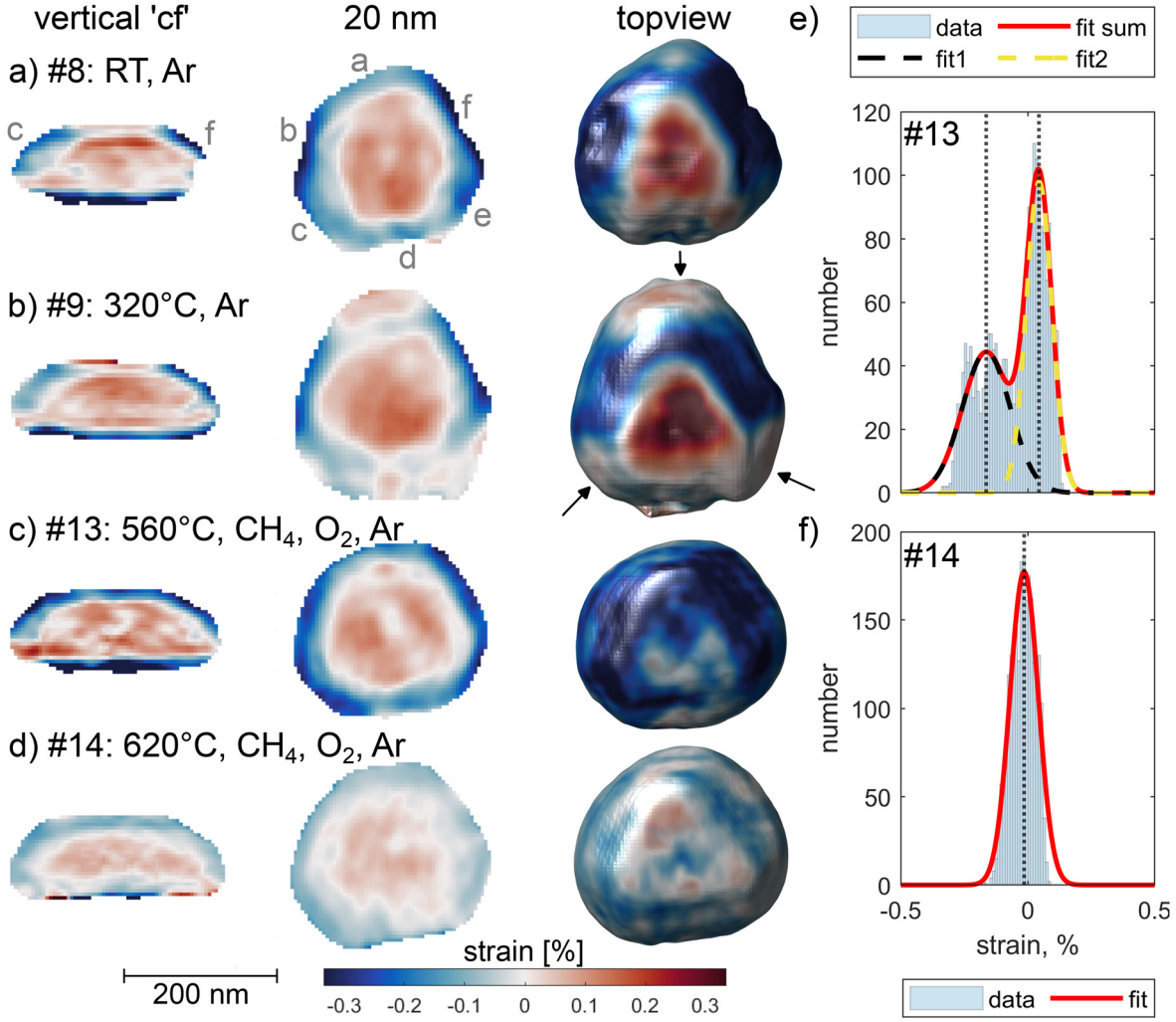

Fig. 4 Cuts through selected datasets on Sample-150 (a) At RT under Ar atmosphere after first exposure to methane oxidation conditions at 470 °C. (b) At 320 °C under Ar atmosphere, after H_2 treatment during the ramp up. The black arrows are pointing towards the {111} oriented facets, where we observed the tensile strain. (c) At 560 °C under methane oxidation conditions. (d) At 620 °C under methane oxidation conditions, the strain is decreasing and the ring structure seems to vanish. (e) Histogram of the strain values from the horizontal cut at 20 nm of the dataset shown in (c). The histogram was fitted using two Gaussians, with the peak positions indicated by the dashed lines at $-(0.163 \pm 0.018)\%$ and $(0.044 \pm 0.005)\%$. (f) Histogram of the strain values from the horizontal cut at 20 nm of the dataset shown in (d). The histogram was fitted using one Gaussian, with the peak position indicated by the dashed line at $(0.015 \pm 0.006)\%$. All datasets are cut as indicated in Fig. 2 and the NP facets are indicated in the same manner. The numbers marked by # denotes the number of the datasets.

shown in SI section S8. Overall, Pt and Pd seem to start alloying at this temperature.

As one can see in Fig. 5 Sample-670 does not show such kind of facet-dependent Pt segregation even at temperatures up to 680 °C (see SI section S9), which might originate from the different initial state.

After applying several cycles of methane oxidation condition with maximal 550 °C and including H_2 treatments (see SI section S9), Sample-670 does not change (Fig. 5a and b) in comparison to the initial state in Fig. 3. Upon increasing the temperature further to 680 °C, the strain distribution is however changing drastically. As shown in (Fig. 5c) a clear ring structure is surprisingly present now, with high tensile strain at the surface (max. 0.35% in horizontal cut) and high compressive strain at the inside (min. −0.37% in horizontal cut, see SI section S8 for the values). This range of the compressive strain values agrees with the calculated compositional strain of $(-0.46 \pm 0.2)\%$ for 100% Pd compared to the calculated lattice constant from the Bragg peak center of this dataset at 680 °C (see SI section S7 for the calculation). The presence of a Pd rich core Pt shell structure is further confirmed by comparing observed features with literature on de-alloying NPs with different materials.[35,36] Especially, the splitting of the strain histogram into two peaks (from Fig. 5f to g) and the increase of the asymmetry in the line profile through the fringes of the intensity distribution around the Bragg peak (shown in SI section S10) are typical for de-alloying.[37,38] Furthermore, the radius $r = (40 \pm 5)$ nm of the region with compressive strain

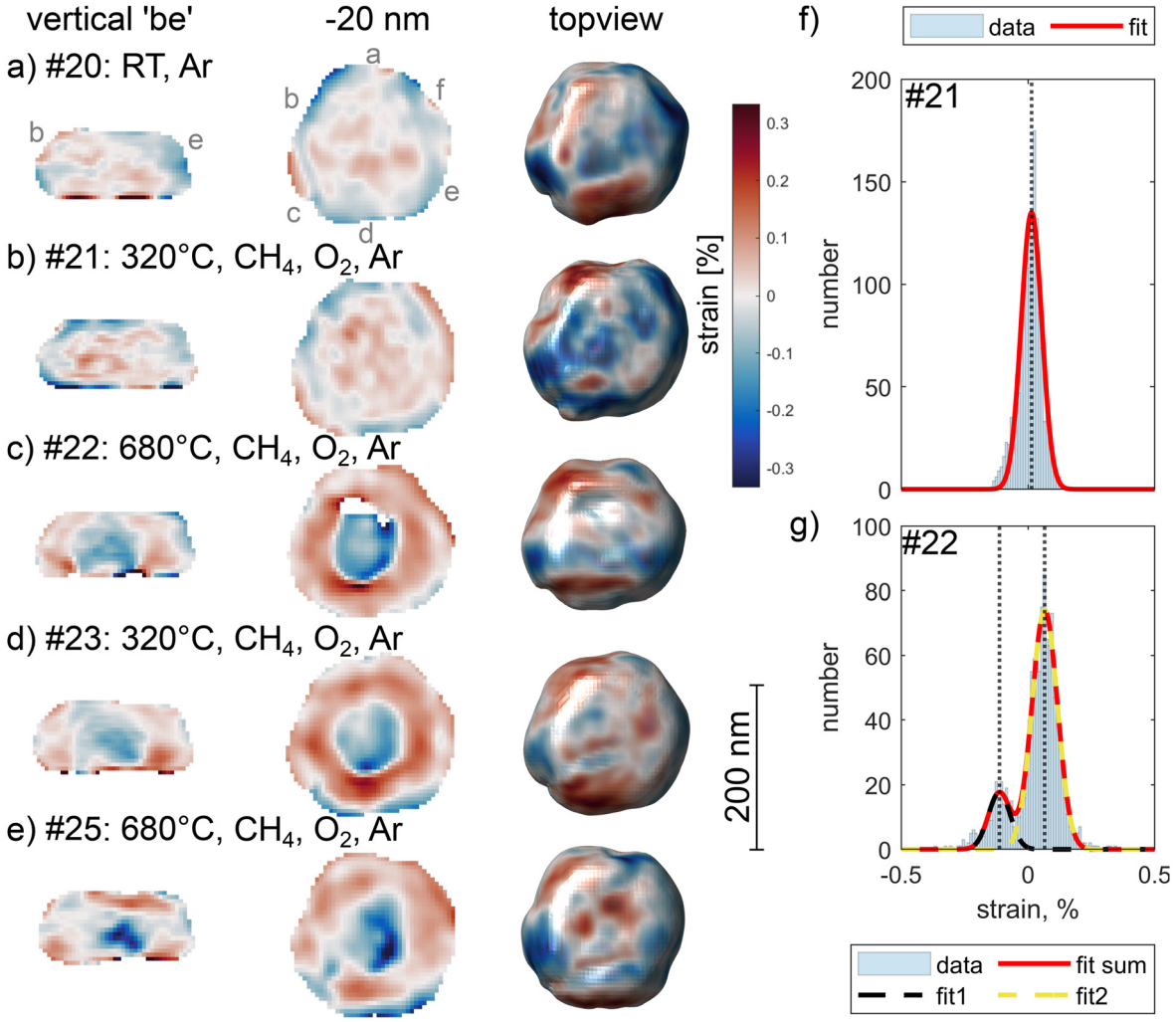

Fig. 5 Cuts through selected datasets on Sample-670 (a) At RT under Ar atmosphere. (b) At 320 °C under methane oxidation conditions. (c) At 680 °C under methane oxidation conditions. (d) At 320 °C under methane oxidation conditions, after switching to Ar atmosphere and then to a H_2 treatment at this temperature, as shown in Supplementary section S9. (e) At 680 °C under methane oxidation conditions. (f) Histogram of the strain values from the horizontal cut at −20 nm shown in (b). The histogram was fitted using one Gaussian, with the peak position indicated by the dashed line at −(0.014 ± 0.057)%. (g) Histogram of the strain values from the horizontal cut at −20 nm shown in (c). The histogram was fitted using two Gaussians, with the peak positions indicated by the dashed lines at −(0.113 ± 0.004)% and (0.066 ± 0.005)%. All datasets are cut as indicated in Fig. 3 and the NP sides are indicated in the same manner. The gaps in the reconstructed shape do not result from real gaps in the NP, but rather from failure in the reconstruction at those points due to high strain values.

agrees with the radius r = 42 nm of a half-sphere filled by the volume the of evaporated Pd, see SI section S11. Altogether one can conclude a Pd rich core, Pt shell structure was formed, thus an inverted core–shell structure compared to the initial state of Sample-150. The Pd rich core, Pt shell structure was not changed by decreasing the temperature and applying an H_2 treatment (see Fig. 5d) and when increasing the temperature to 680 °C for the second time (Fig. 5e).

4 Discussion

In the following, we discuss the factors influencing the segregation leading to a Pd rich core and a Pt shell NP. The temperature plays a key role in this process. Notably, such a structure was not observed in Sample-150, which was only heated to maximal 620 °C during the *in situ* experiment, thus 60 °C lower than the temperature at which the strain changes in Sample-670 occurred. This temperature dependency of the dealloying is inline with the reported temperature dependency of the Pt and Pd segregation. It is reported that Pd starts segregating to the surface for temperatures above 300 °C, while Pt segregates to the surface at temperatures above 700 °C under ultra high vacuum (UHV) conditions.[12] The presence of O_2 or H_2 is increasing this trend, so Pt is segregating to the surface at lower temperatures of around 500 °C – 550 °C. Under O_2 the Pd oxide formation is thereby preventing Pd from moving into the bulk and promotes the Pd segregation to the surface for

temperatures between 300 °C and around 550 °C.[4,8–10,39,40] At 680 °C and 20 mbar O_2 pressure, PdO and Pd surface oxides are thermodynamically not stable, and therefore reduced.[41] The Pt concentration has an important influence on the Pd oxide formation, as it was shown that PdO is less stable with higher Pt concentration.[4] The segregation of Pd to the surface under the presence of O_2 depends on the Pt concentration as well, as it is reduced with higher Pt concentration.[12,42,43] Overall one can conclude, that while the formation of Pd oxide might have hindered the segregation of Pt to the surface at lower temperatures, the observed segregation of Pt to the surface at 680 °C was not induced by oxide formation but by a reduction of the surface energy under the experimental conditions.

Apart from the temperature, the biggest influence is the different initial state. Sample-150 has a Pd shell at the beginning of the *in situ* experiment, due to the lower overgrowth temperature. Thus more Pd has to be transported further into the NP and more Pt to the surface to form a Pt shell Pd rich core structure. Furthermore, we speculate that the higher availability of Pd at the surface has led to more oxidized Pd in Sample-150, which needs to be reduced before Pd can segregate into the bulk. Taking this into account, we assume that the observed mixing of the Pt and Pd on Sample-150 is a first step towards a Pt shell, Pd core like in Sample-670, inline with a core–shell inversion.

Next, we discuss how the initial state and its transformation through segregation and mixing during the *in situ* experiment may influence the catalytic activity. The different initial states of both samples are expected to have a significant impact on the performance. It has been shown in several experiments and simulations, that the core–shell structure of NPs can boost their catalytic activity compared to alloyed NPs of the same materials, since the core–shell structure has a high impact on the strain.[22–25] Such increased strain of the core–shell system, compared to the partially alloyed system was also observed in our experiment. Additionally, the initial core–shell NP might be more stable compared to PtPd alloy NPs, because no mass transport is needed to form Pd oxide. The partially alloyed state on the other hand is not preferential, since the high Pt concentration prevents the formation of Pd oxide, so the catalytic performance may be close to the performance of pure Pt which is lower than the activity of Pd oxide.[4–6]

Furthermore, the segregation and mixing is influencing the catalytic performance of both samples as well. For the initial Pt core, Pd shell Sample-150 it was observed that Pt segregates to {111} oriented facets under methane oxidation conditions at temperatures up to around 520 °C. The existence of Pt segregated to the Pd rich surface might be beneficial for the activity for methane oxidation for partial oxygen pressures up to 25 mbar, above this pressure Pd oxide facets are more preferred sites for methane oxidation.[4] On the other hand, such facet dependent surface composition could be utilized to prepare bifunctional catalyst NPs. In case of the initially partially alloyed Sample-670, we observed Pt segregation to the surface at 680 °C, resulting in a Pd rich core, Pt shell structure. Other than the numerously observed Pd segregation to the surface,[4,8–10] is Pt segregation is not driven by oxide formation but it thermodynamically favored. In contrary, the Pt segregation was promoted because Pd oxide gets reduced at such high temperatures.[4,44] Since Pd is more active than Pt,[4–6,45] this compositional change might have a negative effect on the activity of the NP. Thus, such PtPd alloyed catalyst NPs should only be operated for temperatures below 680 °C for methane oxidation.

5 Conclusion

In this case study, we successfully tuned the initial element distribution from a core–shell to a partially alloyed structure by varying the temperature during the overgrowth of Pd on Pt NPs. Using BCDI, we observed the influence of Pd on Pt near the Pt–Pd interface, confirming the core–shell morphology. During *in situ* measurements under methane oxidation at temperatures between 320 °C and 560 °C, Pt segregated to the {111} oriented facets of the initial core–shell NP. This temperature-dependent segregation could be exploited to control the facet composition based on orientation to prepare bifunctional catalyst NPs. Conversely, Sample-670, the initially partially alloyed NP did not exhibit such facet-dependent segregation; instead we observed the formation of a Pd core, Pt shell structure at 680 °C. Since Sample-150, the initial Pt core, Pd shell sample showed Pd–Pt mixing at 620 °C, we hypothesize that this NP would form such an inverted core–shell structure under higher temperatures as well, thus this maximum operating temperature should not be exceeded. These results demonstrate opportunities for systematically investigating promising core–shell nanoparticle and their catalytic activity, offering valuable insights for the design of advanced catalysts.

Author contributions

Lydia J. Bachmann: data curation; formal analysis; investigation; validation; visualisation; writing – original draft; Jagrati Dwivedi: investigation; Dmitry Lapkin: investigation; Bihan Wang: investigation; Jan-Christian Schober: investigation; Gerard N. Hinsley: investigation; writing – review & editing; Sarah Bernart: investigation; Kuan Hoon Ngoi: investigation; Rustam Rysov: methodology; Arti Dangwal Pandey: data curation; investigation; Thomas F. Keller: conceptualization; investigation; supervision; validation; writing – review & editing; Ivan A. Vartanyants: conceptualization; investigation; supervision; validation; writing – review & editing; Andreas Stierle: conceptualization; funding acquisition; investigation; methodology; project administration; resources; supervision; validation; visualisation; writing – review & editing.

Conflicts of interest

There are no conflicts to declare.

Data availability

Data for this article, including SEM and AFM images, as well as the original BCDI and mass spectrometer datasets are available at https://zenodo.org/records/17642484.

Supplementary information (SI): additional calculations, images and further information. See DOI: https://doi.org/10.1039/d5nr05321h.

Acknowledgements

We acknowledge DESY (Hamburg, Germany), a member of the Helmholtz Association HGF, for the provision of experimental facilities. Parts of this research were carried out at PETRA III and the DESY NanoLab. Data was collected using beamline P10 operated/provided by DESY Photon Science. We would like to thank Michael Sprung for assistance during the experiments. Beamtime was allocated for proposal I-20220472 (beamtime number 11014909) and an in-house beamtime (beamtime number 11013316). This work was supported by the European Union within the EU H2020 framework program for research and innovation under grant no. 101007417 Nanoscience Foundries and Fine Analysis (NFFA-Europe-Pilot). This work was supported by the Deutsche Forschungsgemeinschaft, Germany (DFG, German Research Foundation) *via* SFB 1441, Project-ID 426888090. The authors thank A. Jeromin and S. Kulkarni for performing the SEM and EDX measurements and the FIB preparation. We acknowledge the use of the CHyN cleanroom facility, jointly operated by UHH, DESY, and MPSD. We thank B. Bosnjak for performing the e-beam lithography process.

References

1 P. Forster, *et al.*, in *Climate Change 2021: The Physical Science Basis. Contribution of Working Group I to the Sixth Assessment Report of the Intergovernmental Panel on Climate Change*, ed. V. Masson-Delmotte, *et al.*, Cambridge University Press, Cambridge, United Kingdom and New York, NY, USA, 2021, pp. 923–1054.

2 A. Trinchero, A. Hellman and H. Grönbeck, Methane oxidation over Pd and Pt studied by DFT and kinetic modeling, *Surf. Sci.*, 2013, **616**, 206–213.

3 H. Lott, M. Casapu, J.-D. Grunwaldt and O. Deutschmann, A review on exhaust gas after-treatment of lean-burn natural gas engines – From fundamentals to application, *Appl. Catal. B*, 2024, **340**, 123241pp.

4 W. Qi, *et al.* Methane combustion reactivity during the metal→metallic oxide transformation of Pd-Pt catalysts: Effect of oxygen pressure, *Appl. Surf. Sci.*, 2018, **435**, 776–785.

5 E. D. Goodman, *et al.*, Uniform Pt/Pd Bimetallic Nanocrystals Demonstrate Platinum Effect on Palladium Methane Combustion Activity and Stability, *ACS Catal.*, 2017, **7**, 43724380.

6 J. Park, *et al.*, Impact of Pd : Pt ratio of Pd/Pt bimetallic catalyst on CH4 oxidation, *Appl. Catal., B*, 2022, **316**, 121623.

7 K. Persson, K. Jansson and S. G. Järås, Characterisation and microstructure of Pd and bimetallic Pd–Pt catalysts during methane oxidation, *J. Catal.*, 2007, **245**, 401–414.

8 F. Tao, *et al.*, Reaction-Driven Restructuring of Rh-Pd and Pt-Pd Core-Shell Nanoparticles, *Science*, 2008, **322**, 932–934.

9 H. Nie, J. Y. Howe, P. T. Lachkov and Y.-H. C. Chin, Chemical and Structural Dynamics of Nanostructures in Bimetallic PtPd Catalysts, Their Inhomogeneity, and Their Roles in Methane Oxidation, *ACS Catal.*, 2019, **9**, 54455461.

10 W. Qi, *et al.*, Kinetic consequences of methane combustion on Pd, Pt and Pd–Pt catalysts, *RSC Adv.*, 2016, **6**, 109834–109845.

11 J.-D. Grunwaldt, N. van Vegten and A. Baiker, Insight into the structure of supported palladium catalysts during the total oxidation of methane, *ChemComm*, 2007, 4635–4637.

12 L. C. A. Van den Oetelaar, *et al.*, Surface Segregation in Supported Pd-Pt Nanoclusters and Alloys, *J. Phys. Chem. B*, 1998, **102**, 3445–3455.

13 C. Chatelier, *et al.*, Unveiling CoreShell Structure Formation in a Ni3Fe Nanopar- ticle with In Situ Multi-Bragg Coherent Diffraction Imaging, *ACS Catal.*, 2024, **18**, 13517–13527.

14 S. Fernandez, *An insight into nanostructures through coherent diffraction imaging*, PhD thesis, Universit'e de Marseille, vol. **20**, 2016.

15 D. Mukherjee, J. T. L. Gamler, S. E. Skrabalak and R. R. Unocic, Lattice Strain Measurement of Core@Shell Electrocatalysts with 4D Scanning Transmission Electron Microscopy Nanobeam Electron Diffraction, *ACS Catal.*, 2020, **10**, 55295541.

16 Y. Y. Kim, *et al.*, Single alloy nanoparticle X-ray imaging during a catalytic reaction, *Sci. Adv.*, 2021, **7**, 1–8.

17 I. Robinson and R. Harder, Coherent X-ray Diffraction Imaging of Strain at the Nanoscale, *Nat. Mater.*, 2009, **8**, 291–298.

18 I. A. Vartanyants and O. M. Yefanov, in *X-Ray Diffraction: Modern Experimental Techniques*, ed. O. H. Seeck and B. M. Murphy, Pan Stanford Publishing Pte. Ltd, 2015, pp. 341–384.

19 J. Miao, T. Ishikawa, I. K. Robinson and M. M. Murnane, Beyond crystallogra- phy: Diffractive imaging using coherent X-ray light sources, *Science*, 2015, **348**, 530–535.

20 M. C. Newton, S. J. Leake, R. Harder and I. K. Robinson, Three-dimensional imaging of strain in a single ZnO nanorod, *Nat. Mater.*, 2009, **9**, 120–124.

21 Y. Sun and A. Singer, Bragg Coherent diffractive imaging for defect analysis: Principles, applications, and challanges, *Chem. Phys. Rev.*, 2024, **5**, 031310.

22 M. Li, *et al.*, Exclusive Strain Effect Boosts Overall Water Splitting in PdCu/Ir Core/Shell Nanocrystals, *Angew. Chem., Int. Ed.*, 2021, **60**, 8243–8250.

23 P. Moseley and W. A. Curtin, Computational Design of Strain in CoreShell Nanoparticles for Optimizing Catalytic Activity, *Nano Lett.*, 2015, **15**, 40894095.
24 P. Strasser, *et al.*, Lattice-strain control of the activity in dealloyed core–shell fuel cell catalysts, *Nat. Chem.*, 2010, **2**, 454–460.
25 Y. Li, *et al.*, Synthesis of bimetallic Pt-Pd core-shell nanocrystals and their high electrocatalytic activity modulated by Pd shell thickness, *Nanoscale*, 2012, **3**, 845.
26 G. Koster, B. L. Kropman, G. J. H. M. Rijnders, D. H. A. Blank and H. Rogalla, Quasi-ideal strontium titanate crystal surfaces through formation of strontium hydroxide, *Appl. Phys. Lett.*, 1998, **73**, 2920.
27 T. F. Keller, *et al.*, Coherent X-ray diffraction of a semiregular Pt nanodot array, *Phys. Rev. B*, 2023, **108**, 134109.
28 H. Noei, V. Vonk, T. F. Keller, R. Röhlsberger and A. Stierle, DESY NanoLab, *Journal of large-scale research facilities*, 2016, **2**, A76.
29 D. Weschke, Methodische Entwicklung von Experimentkomponenten für einen 6-Kreis-Diffraktometer-Aufbau, Available at https://hdl.handle.net/20.500.12738/6135. Bachelor's thesis (Hochschule für Angewandte Wissenschaften Hamburg, Apr. 2013).
30 D. Dzhigaev, 2021. https://github.com/dzhigaevd/phasor.
31 M. Abuin, *et al.*, Coherent X-ray Imaging of CO-Adsorption-Induced Structural Changes in Pt Nanoparticles: Implications for Catalysis, *ACS Appl. Nano Mater.*, 2019, **2**, 4818–4824.
32 M. Nathanson, K. Kanhaiya, A. Pryor Jr, J. Miao and H. Heinz, Atomic-Scale Structure and Stress Release Mechanism in CoreShell Nanoparticles, *ACS Nano*, 2018, **12**, 12296–12304.
33 J. Zhao, B. Chen and F. Wang, Shedding Light on the Role of Misfit Strain in Controlling Core–Shell Nanocrystals, *Adv. Mater.*, 2020, **32**, 2004142.
34 D. S. Dolling, *et al.*, Probing Active Sites on Pd/Pt Alloy Nanoparticles by CO Adsorption, *ACS Catal.*, 2024, **18**, 13517–13527.
35 T. Kawaguchi, *et al.*, Gas-Induced Segregation in Pt-Rh Alloy Nanoparticles Observed by In Situ Bragg Coherent Diffraction Imaging, *Phys. Rev. Lett.*, 2019, **123**, 246001.
36 T. Kawaguchi, *et al.*, Electrochemically Induced Strain Evolution in Pt–Ni Alloy Nanoparticles Observed by Bragg Coherent Diffraction Imaging, *Nano Lett.*, 2021, **21**, 5945–5951.
37 W. Cha, Y. Liu, H. You, G. B. Stephenson and A. Ulvestad, Dealloying in Individual Nanoparticles and Thin Film Grains: A Bragg Coherent Diffractive Imaging Study, *Adv. Funct. Mater.*, 2017, **27**, 1700331.
38 S. T. Haag, *et al.*, Anomalous coherent diffraction of core-shell nano-objects: A methodology for determination of composition and strain fields, *Phys. Rev. B:Condens. Matter Mater. Phys.*, 2013, **87**, 035408.
39 R. Huang, Y.-H. Wen, Z.-Z. Zhu and S.-G. Sun, PtPd Bimetallic Catalysts: Structural and Thermal Stabilities of CoreShell and Alloyed Nanoparticles, *J. Phys. Chem. C*, 2012, **116**, 86648671.
40 K. Matsumoto, M. Hiyoshi, T. Iijima, H. Noguchi and K. Uosaki, Investigation of the effects of Pt/Pd composition and PVP content on the activity of Pt/Pd core-shell catalysts, *Electrochem. Commun.*, 2020, **115**, 106736.
41 N. Kasper, P. Nolte and A. Stierle, Stability of Surface and Bulk Oxides on Pd(111) Revisited by in Situ X-ray Diffraction, *J. Phys. Chem. C*, 2012, **116**, 2145921464.
42 E. D. Goodman, *et al.*, Palladium oxidation leads to methane combustion activity: Effects of particle size and alloying with platinum, *J. Chem. Phys.*, 2019, **151**, 154703.
43 A. Dianat, *et al.*, Ab initio study of element segregation and oxygen adsorption on PtPd and CoCr binary alloy surfaces, *Surf. Sci.*, 2008, **602**, 876–884.
44 J.-C. Schober, *Operando Investigations of Structure-Activity Relationships in Pd-based Model Catalysts for Methane Oxidation*, PhD thesis, University of Hamburg, 2025.
45 X. Weng, H. Ren, M. Chen and H. Wan, Effect of Surface Oxygen on the Activation of Methane on Palladium and Platinum Surfaces, *ACS Catal.*, 2014, **4**, 25982604.